Anatomy and paleofluid evolution of laterally restricted extensional fault zones in the Jabal Qusaybah anticline, Salakh arch, Oman

Geological Society of America Bulletin, published online on 10 February 2016 as doi:10.1130/B31317.1

Anatomy and paleofluid evolution of laterally restricted extensional fault zones in the Jabal Qusaybah anticline, Salakh arch, Oman

F. Balsamo[1,†], L. Clemenzi[1], F. Storti[1], M. Mozafari[2], J. Solum[3], R. Swennen[2], C. Taberner[3], and C. Tueckmantel[3]
[1]*Natural and Experimental Tectonics Research Group (NEXT), Department of Physics and Earth Sciences "Macedonio Melloni," University of Parma, 43124, Parma, Italy*
[2]*Geology Department of Earth and Environmental Sciences, KU Leuven, B-3001 Leuven, Belgium*
[3]*Carbonate Research Team, Shell Global Solutions International, 2288 GS Rijswijk, The Netherlands*

ABSTRACT

The E-W–trending Jabal Qusaybah anticline, at the western termination of the Salakh arch, Oman Mountains, is characterized by a complex fault network that developed in layered Cretaceous carbonates. This network includes NE-SW left-lateral, N-S extensional, and subordinate E-W extensional fault zones. The N-S–striking extensional faults zones are roughly perpendicular to the fold axis and are best developed in the longitudinally bulged central sector of the anticlinal crest. They are likely due to along-strike outer-arc extension associated with positive fault inversion and salt migration. These extensional fault zones are confined within, and locally abut, major NE-SW left-lateral strike-slip fault zones. Extensional fault displacements range between a few decimeters and ~60 m, whereas the maximum exposed trace lengths range between a few meters and ~800 m. Narrow (~1–15-cm-thick) cataclastic fault cores are surrounded by vein-dominated damage zones as thick as tens of meters. Moreover, fault zones show widespread evidence for substantial dilation in the form of (1) dilation breccias, (2) infilling by large columnar calcite crystals and aggregates, and (3) centimeter- to meter-thick veins. Dilation breccias and calcite infillings are primarily localized at fault tips, fault overlaps, and interaction zones between strike-slip and extensional fault segments. Displacement profiles along the N-S–striking extensional fault zones indicate that they are one order of magnitude shorter than values predicted by most published displacement-length scaling laws. By analyzing fault abutting geometries, detailed vein relative chronology, $\delta^{13}C$ and $\delta^{18}O$ signatures, and fluid inclusion data from calcite veins and calcite fault infillings, we propose a model whereby a deep-seated, regionally sized, left-lateral strike-slip fault system that was active during anticline growth inhibited the lateral propagation of late-stage transversal extensional fault zones. Our findings show that, in this geological setting, the structural position, rather than fault displacement, is the parameter controlling the location of the more dilatants (and permeable) fault segments. Results of the present work suggest that fault intersections may be more useful than fault throw for predicting zones of enhanced vertical fluid flow in structurally complex carbonate reservoirs.

INTRODUCTION

Extensional fault zones are ubiquitous structures in all tectonic settings. Growth models and geometrical properties of extensional fault zones have been extensively studied in a variety of lithologies and geological contexts (Walsh and Watterson, 1987; Childs et al., 2003; Soliva et al., 2005; Balsamo and Storti, 2010; Torabi and Berg, 2011; Schultz et al., 2013). In fold-and-thrust belts, syncontractional extensional faults typically form parallel to fold axes during folding-related outer-arc extension (e.g., Lisle, 1994; Tavani et al., 2015). The study of geometrical attributes of fault zone populations (i.e., fault core and damage zone width, fault length, maximum displacement, and displacement profiles along fault zones) is of great importance, not only to estimate the spatial distribution of deformation in a region (Scholz and Cowie, 1990; Rotevatn and Bastesen, 2014) and to develop models for fault growth (e.g., Cowie and Scholz, 1992; Tondi et al., 2012; Schultz et al., 2013), but also to provide scaling laws that may help to predict fracture distributions in hydrocarbon reservoirs and groundwater aquifers (e.g., Fossen and Hesthammer, 1997; Ortega et al., 2006). Scaling relationships between fault displacement and length are generally employed to assess the long-term behavior and growth history of fault zones (e.g., Kim and Sanderson, 2005). Departures from ideal conditions can be used to make inferences on processes such as fault growth by segment interaction and linkage (e.g., Cartwright et al., 1995), and fault restriction due to mechanical boundaries caused by changes in stratigraphy (Soliva and Benedicto, 2005; Soliva et al., 2005; Wilkins and Gross, 2002).

In this contribution, we describe the structural architecture, geometric attributes, and paleofluid evolution of laterally restricted extensional fault zones that developed during the growth of the Jabal Qusaybah anticline (Salakh arch, Oman). Both strike-slip and extensional fault systems focused, at different stages, precipitation of significant volumes of calcite cement in fracture networks and brecciated rocks. The main objectives of this contribution are the following: (1) to document the structural architecture of both strike-slip and extensional fault zones; (2) to provide new geometrical attributes for compartmentalized, laterally restricted extensional fault zones in layered carbonates; and (3) to link the overall structural framework with the spatial distribution of dilation breccias, cement petrography, and geochemistry of the mineralizing fluids. The integration of these data sets, combined with the comparison of literature data on fault zone attributes from other extensional settings, allows reconstruction of the main stages of the coupled fault growth and fluid evolution history associated with fold amplification.

GEOLOGICAL SETTING AND STRATIGRAPHY

The Oman Mountains are located on the eastern margin of the Arabian Platform and form an ~650-km-long mountain chain (Fig. 1A). From the Late Cretaceous to the present,

[†]fabrizio.balsamo@unipr.it

 doi: 10.1130/B31317.1; 16 figures; 1 table; Data Repository item 2016050.

Geological Society of America Bulletin, published online on 10 February 2016 as doi:10.1130/B31317.1

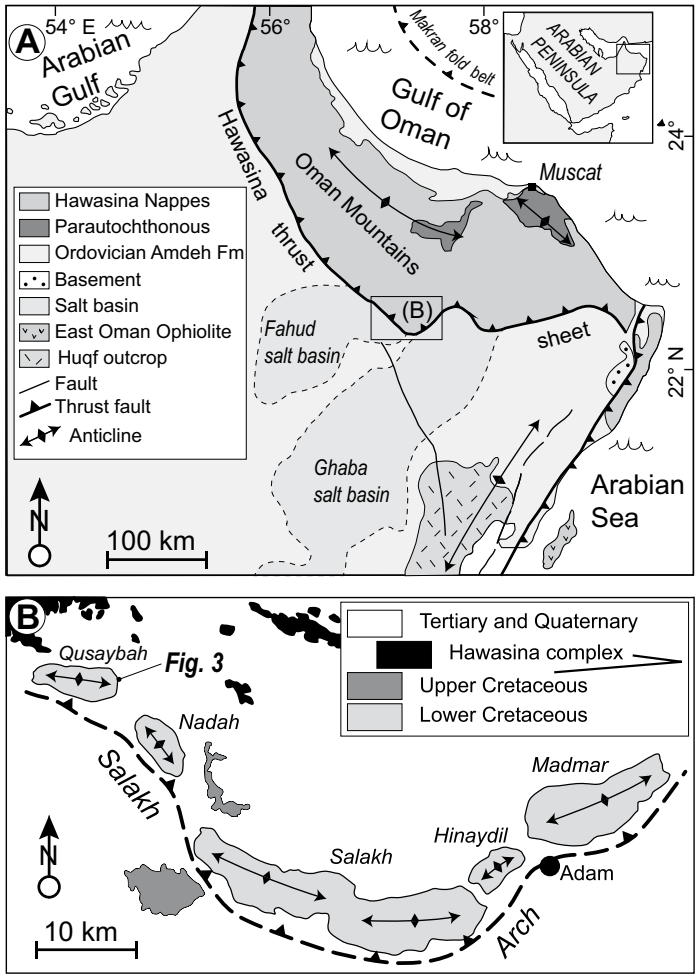

Figure 1. (A) Simplified geological map showing the location of the study area at the southern deformation front of the Oman Mountains (modified from Al-Kindi, 2006; Filbrandt et al., 2006). (B) Schematic geological map of the Salakh arch, northern Oman, showing the E-W–trending Jabal Qusaybah anticline.

the construction of the Oman Mountains chain has taken place in the context of the closure of the eastern Neotethys ocean, which involved approximately N-S convergence of the Eurasia-Iran and Africa-Arabia continental blocks, with southwestward thrusting of the Hawasina complex and the Semail ophiolite onto the Arabian Platform (Warburton et al., 1990, and references therein). The Jabal Qusaybah anticline is located in the Salakh arch, at the southern deformation front of the northern Oman Mountains (Figs. 1A and 1B). There, the complete stratigraphic succession includes Precambrian carbonates and siliciclastic rocks, Paleozoic mostly siliciclastic rocks containing the Early Cambrian Ara evaporites, and Mesozoic to Cenozoic carbonates with interlayered siliciclastics (Mount et al., 1998; Richard et al., 2014). The Cretaceous stratigraphic succession begins with the platform carbonates of the Kahmah Group. A regional unconformity separates these carbonates from the shales and sandstones of the Nahr Umr Formation; another unconformity separates the latter from the Natih Formation. The upper part of the Natih Formation is eroded and unconformably overlain by the shales and sandstones of the Aruma Group (Fig. 2; e.g., Homewood et al., 2008). The Natih Formation, consisting of seven lithostratigraphic members (e.g., Homewood et al., 2008, and references therein), is among the most prolific subsurface carbonate reservoirs of North Oman (Al-Kindi and Richard, 2014; Arndt et al., 2014; Richard et al., 2014).

In Jabal Qusaybah, the Cenomanian–Turonian members of the Natih Formation crop out (Fig. 2B). The A member (late Cenomanian–early Turonian) is exposed along the entire anticline and primarily consists of platform carbonates. The B member (middle–late Cenomanian), widely exposed along the flanks of N-S wadies (dry channels) cutting the central sector of the anticline, consists of intrashelf basinal organic-rich carbonates. A more competent organic-rich horizon, named B_3 (Homewood et al., 2008), occurs within Natih B (Fig. 2B) and provides a useful key horizon for stratigraphic correlations and determination of fault offset. The C member (early Cenomanian) crops out only at the bottom of eroded valleys in the central sector of the fold, and it consists primarily of platform carbonates characterized by a yellowish horizon of coarse-grained rudist debris forming a tidal sandwave (e.g., Hanna and Smewing, 1996; Homewood et al., 2008) overlying an ~5-m-thick, intensely bioturbated mudstone layer, and layered carbonates.

Structural Framework of the Jabal Qusaybah Anticline

Jabal Qusaybah is an ~8-km-long and 3-km-wide anticline developed by positive inversion of an early Turonian extensional fault zone (Fig. 3), which possibly involved the Ara salt as a basal décollement layer (Storti et al., 2015). The hinge line of the Jabal Qusaybah anticline strikes approximately E-W, the exposed cross-sectional fold shape is open, and overall it is slightly asymmetrical to the north. The anticline is characterized by a complex deformation pattern acquired during progressive fold growth and exhumation (Storti et al., 2015). The most prominent structural features are NE-SW, left-lateral strike-slip fault zones trending oblique to the fold-axis, and fold-perpendicular, N-S extensional fault zones located in the central sector of the fold (Fig. 3). The latter features are associated with late-stage, salt-cored axial bulging and dilation in the central region of the anticlinal crest (Storti et al., 2015). Many left-lateral strike-slip fault zones show higher displacement values when approaching the northern termination of the exposed fold backlimb, indicating that they extend northward below the Quaternary alluvial deposits. Conversely, the N-S extensional fault zones are mostly confined by the strike-slip fault zones. In places, N-S extensional fault zones develop at the southwestern tip of the left-lateral strike-slip fault zones and terminate within the anticline. As a whole, the fault network forms a left-lateral, transtensional horsetail array localized in the longitudinal axial bulge of the fold anticline (Fig. 3; Storti et al., 2015).

The present study focused on an ~1-km-wide × 3-km-long area located in the central part of the fold, in which structures associated

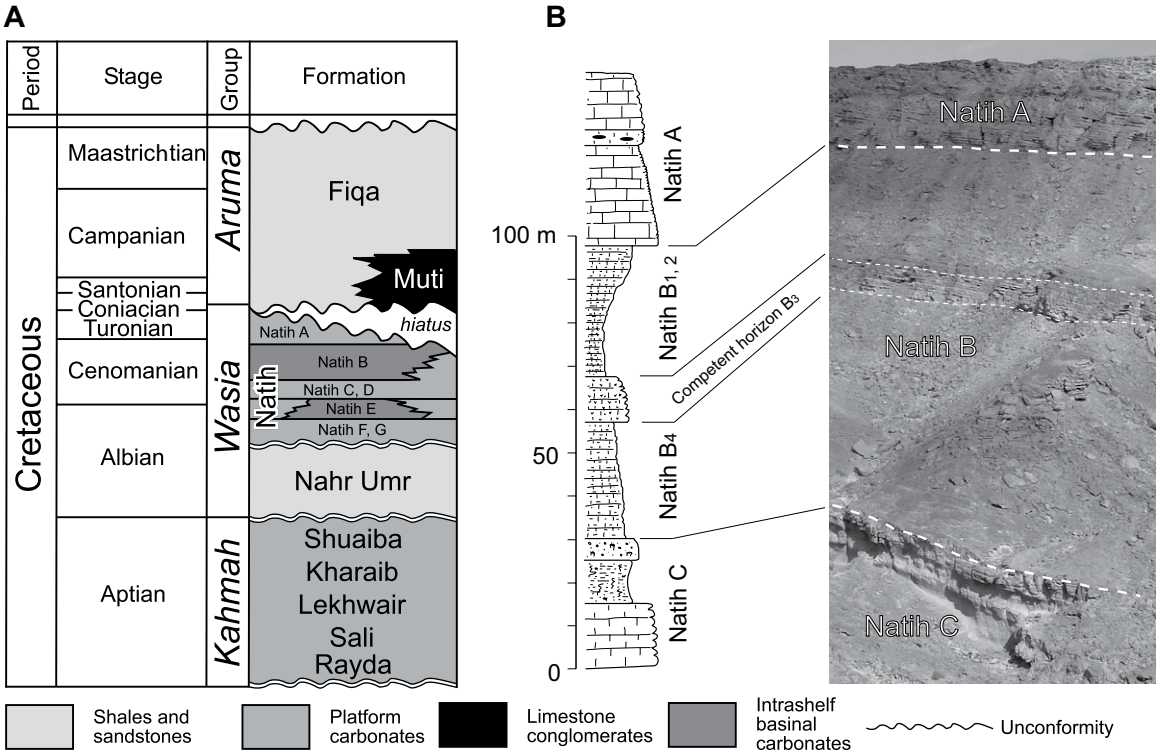

Figure 2. (A) Stratigraphic column of the Cretaceous rocks exposed in the Oman Mountains (after Filbrandt et al., 2006; Homewood et al., 2008). (B) Stratigraphic column of Natih A to C members exposed in the Jabal Qusaybah anticline.

with both strike-slip and extensional faulting are best exposed in the Natih A to C members (Fig. 3). There, the strike-slip and extensional fault zones, as well as the spatial distribution of brecciated rocks, have been mapped in detail. Furthermore, vein attitude data and fault geometrical attributes have also been collected.

METHODS

We have combined detailed field mapping of fault zones at a scale of 1:400 with microstructural, petrographic, and stable isotope analyses, and fluid inclusion data of fault-related veins and fault-core infillings associated with strike-slip and extensional fault zones. Structural data have been collected in 68 field sites (see online Data Repository DR1[1]). Statistical analyses were performed using the Daisy3 software package (Salvini, 2015), according to the procedure described in Storti et al. (2006). We have also acquired data on maximum fault horizontal trace lengths (L), fault core and damage zone thicknesses (T_{FC}, T_{DZ}, respectively), maximum fault displacements (D_{max}), and along-strike displacement distributions in five selected fault zones named faults 1–5 (see Fig. 4).

A detailed petrographic description of vein and fault-core infillings is beyond the scope of this paper and is presented in a separate companion paper (Mozafari et al., 2015). A selection of 13 representative samples, collected in fault damage zone veins, breccias, and fault infillings, is described to document the main petrographic features, isotopic data, and fluid inclusion data. Sampling from veins is as follows: Three samples are from extensional fault zone 1 (samples JQ2_178, JQ3_008B, JQ3_008D), four are from extensional fault zone 3 (samples JQ2_071, JQ2_072, JQ3_29B, JQ3_29C), and one sample is from fault zone 4 (sample JQ2_077). Sampling from breccias and fault-core infillings is as follows: Two samples are from fault zone 1 (samples JQ2_174, JQ3_005), one sample is from minor transtensional fault splays in the tip region of left-lateral strike-slip fault zones (sample JQ3_027), and one other sample was collected from infillings within a strike-slip fault core (sample

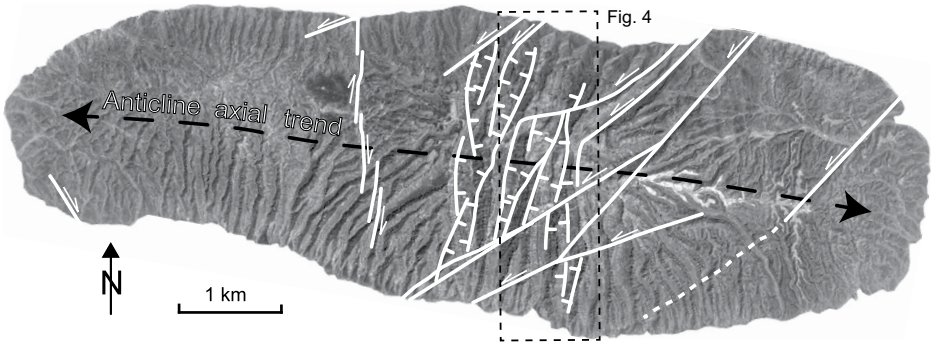

Figure 3. Network of major fault zones mapped in Jabal Qusaybah (modified from Storti et al., 2015). Base map by © 2015 DigitalGlobe; © 2015 Google Earth.

[1]GSA Data Repository item 2016050, structural map of the studied sector in the Jabal Qusaybah anticline, Sultanate of Oman, is available at http://www.geosociety.org/pubs/ft2016.htm or by request to editing@geosociety.org.

Geological Society of America Bulletin, published online on 10 February 2016 as doi:10.1130/B31317.1

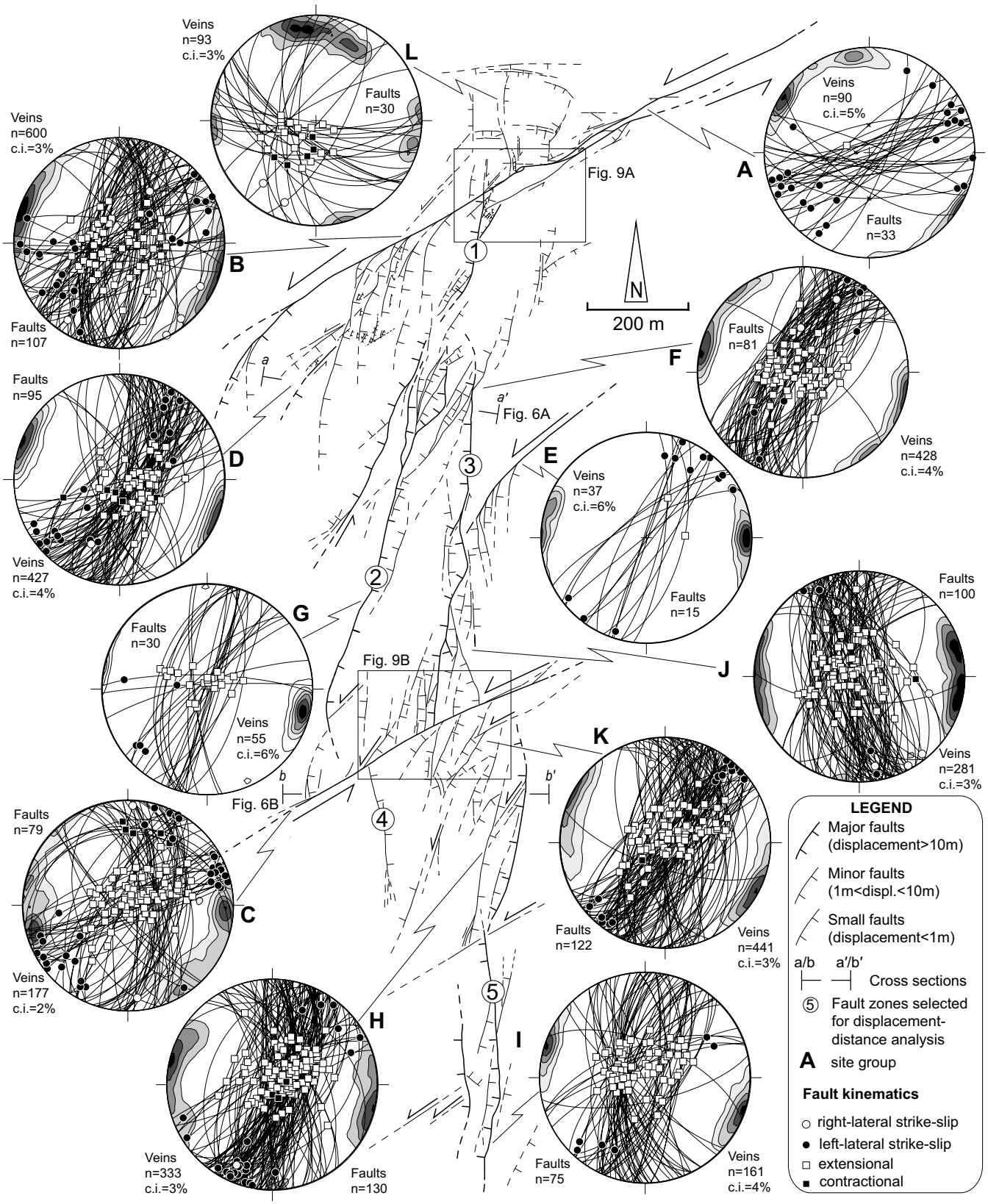

Figure 4. Simplified structural map of the central part of Jabal Qusaybah anticline, based upon 1:400 scale geological mapping, showing the interplay between NE-SW left-lateral strike-slip fault zones and approximately N-S extensional fault zones. The original structural map is available in Data Repository DR1 (see text footnote 1). Stereographic projections (Schmidt net, lower hemisphere) show fault surfaces and contoured pole to veins (c.i.—contouring interval).

Geological Society of America Bulletin, published online on 10 February 2016 as doi:10.1130/B31317.1

JQ3_024). Iron content in polished rock slabs and thin sections was evaluated by using Alizarine Red S and potassium ferricyanide staining (Dickson, 1966). Samples for stable oxygen and carbon isotope analysis were collected employing both a dental drill and a Merkantec micromilling device. The $\delta^{13}C$ and $\delta^{18}O$ values of micromilled and drilled samples were measured at the Vrije Universiteit Amsterdam (the Netherlands) and the Friedrich-Alexander-Universität (Erlangen-Nürnberg, Germany) using Finnigan DeltaPlus isotope-ratio mass spectrometer (IRMS) and ThermoFinnigan 252 mass spectrometer, respectively. Analyses were performed by adding acid (100% H_3PO_4) to the carbonate at a constant temperature of 70 °C. A CO_2 reference gas with known isotopic ratio, also analyzed during the measurements, was used to determine the $\delta^{13}C$ and $\delta^{18}O$ values of the samples. At the Vrije Universiteit Amsterdam, IAEA-CO1 was measured as a control standard. The long-term reproducibility of the measurements of the control standards for $\delta^{13}C$ and $\delta^{18}O$ was <0.1‰ and <0.2‰, respectively. At Friedrich-Alexander-Universität, NBS19 was measured as a standard by assigning a $\delta^{13}C$ value of +1.95‰ and a $\delta^{18}O$ value of –2.20‰. Reproducibility was better than 0.04‰ for $\delta^{13}C$ and 0.05‰ for $\delta^{18}O$. All values are reported in per mil, relative to Vienna Peedee belemnite (VPDB). Obtained $\delta^{18}O$ values were also converted into Vienna standard mean ocean water (VSMOW) notation with the following equation: $\delta^{18}O\_SMOW = 1.03086 \times \delta^{18}O\_VPDB + 30.86$ (Friedman and O'Neil, 1977). Three samples were measured in both laboratories to cross-check if different applications had significant effects on obtained values. Duplicate samples showed a reproducibility better than 0.1‰ and 0.2 ‰ for $\delta^{13}C$ and $\delta^{18}O$, respectively. Composition of parent fluid associated with calcite precipitation was computed from calcite composition and trapping temperature under the assumption of equilibrium precipitation, using the equation $10^3 \times \ln\alpha = (A \times 10^6/T^2) + B$, with A = 2.78 and B = –2.89 (Friedman and O'Neil, 1977).

The aqueous inclusions of six representative samples were examined microthermometrically following the procedures described in detail by Roedder (1984) and Goldstein and Reynolds (1994) using Linkam THMSG-600 and Linkam MDS-600 heating-freezing stages calibrated with SynFlinc synthetic standards and mounted on Olympus BX60 and Olympus BX51 microscopes, respectively. Homogenization temperatures (T_h) of biphase aqueous inclusions were not pressure-corrected and were used as an indication of the minimum trapping temperatures.

STRUCTURAL DATA

Structural Architecture

The structural architecture of the studied fault network is illustrated in Figure 4 (a higher-resolution map on a satellite image with 5 m topographic contouring is available in the online Data Repository DR1 [see footnote 1]). Two major, NE-SW–oriented, left-lateral strike-slip fault zones and numerous approximately NNE-SSW extensional fault zones crosscut all the exposed members of the Natih Formation (Figs. 5A and 5B). The strike-slip fault zones are exposed in the northern (sites A and B in Fig. 4) and central (site C in Fig. 4) sectors of the study area. Pure strike-slip slickenlines are dominant along the major strike-slip fault segments, although oblique-extensional movements are also common (see stereographic projections for sites A–C). In map view, the exposed fault trace lengths of these fault zones exceed 3–4 km (Fig. 3). The maximum net slip of the northern and southern fault zones are 41 and 34 m, respectively. The SW tip of the northern left-lateral strike-slip fault zone shows a horsetail geometry characterized by NNE-SSW transtensional splay fault zones (site D in Fig. 4). Subsidiary strike-slip fault zones with displacements <10 m are present in the central (site E) and southern sectors of the study area, respectively. Horsetail terminations are also common along the latter minor fault zones. Collectively, azimuthal Gaussian distribution statistical analysis of the strike-slip fault zones indicates two main peaks at 33.1°E ± 11.8° (synthetic shear surfaces) and 64.7°E ± 9.8° (main fault surfaces), respectively (Fig. 6A).

Extensional fault zones are very common in the study area and have net slip values ranging from a few decimeters up to ~53 m (Fig. 4). Their average azimuth is 12.5°E ± 19.8° (Fig. 6B). Major extensional fault zones with displacement values >10 m are localized within the crestal sector of the fold anticline, i.e., in the central part of the study area (Figs. 3 and 4). Some of them splay from, or abut against, the NE-SW strike-slip fault zones (i.e., northern terminations of fault zones 1 and 4, southern termination of fault zone 3; Figs. 4 and 5A). In the vicinity of the strike-slip fault zones, the strike of extensional fault zones becomes more variable and ranges from NNW-SSE (site J) to NE-SW (site K). Extensional fault zones also occur as completely isolated segments (faults 2 and 5 in Fig. 4, among others). In many cases, the extensional fault tip regions are systematically characterized by subsidiary splay faulting and fault zone widening (i.e., the northern and southern terminations of fault zone 2, the southern terminations of faults 1 and 4, the northern termination of fault 3; Fig. 4). Such minor splay faults have displacement generally <1–2 m, are oriented roughly parallel to the main fault, and show pure to oblique extensional kinematics. Subsidiary extensional fault zones with displacement values <10 m are dominant in both the northern and southern sectors of the study area, outside the strike-slip–bounded compartments. Overall, the number of extensional fault zones decreases moving away from the crestal sector toward the northern and southern fold limbs.

Along E-W–oriented vertical cross sections, extensional fault zones are generally characterized by the absence of rollover structures or significantly tilted hanging-wall blocks (Fig. 5B). The two cross sections shown in Figure 7 display the structural architecture in the crestal sector of the anticline, which consists of downthrown blocks along conjugate, steeply dipping, planar fault segments (average dip value of 75.7° ± 11.1°; Fig. 7C).

Fault Zone Structure

Both strike-slip and extensional fault zones consist of narrow fault cores, which accommodated most of the slip, surrounded by vein-dominated damage zones (Fig. 8A; Caine et al., 1996). Fault cores consist of centimeter- to decimeter-thick cemented monogenic cataclasites, polished master slip surfaces, and synthetic shear planes (Fig. 8B). Polished slip surfaces locally show multiple sets of slickenfibers indicating downdip to oblique-slip motions, commonly overprinted by strike-slip kinematics (Fig. 8C), particularly at extensional fault tips. Damage zones consist of arrays of subvertical, millimeter- to centimeter-thick veins (Fig. 4) that strike subparallel to the main slip surfaces pertaining to extensional fault zones (Fig. 8D) and form an angle of 30°–40° with respect to master slip surfaces pertaining to the left-lateral strike-slip fault zones (Fig. 8E). Within the regions of strike-slip fault tips (sites D and E in Fig. 4), millimeter- to centimeter-thick calcite veins strike approximately N-S to NNE-SSW, i.e., subparallel to the transtensional splay fault zones. Statistical analysis of vein azimuth indicates a main Gaussian peak at 18.4°E ± 21.2° (Fig. 6C), with a slight asymmetric distribution toward the NE direction (Fig. 6D). Vein frequency systematically increases approaching fault cores in both strike-slip and extensional fault zones.

Fault zones are typically associated with cohesive, coarse carbonate breccia bodies interposed between fault cores and damage zones. Their thickness varies significantly, both along fault strike and dip, ranging between ~10 cm and ~7 m, and with brecciation intensity

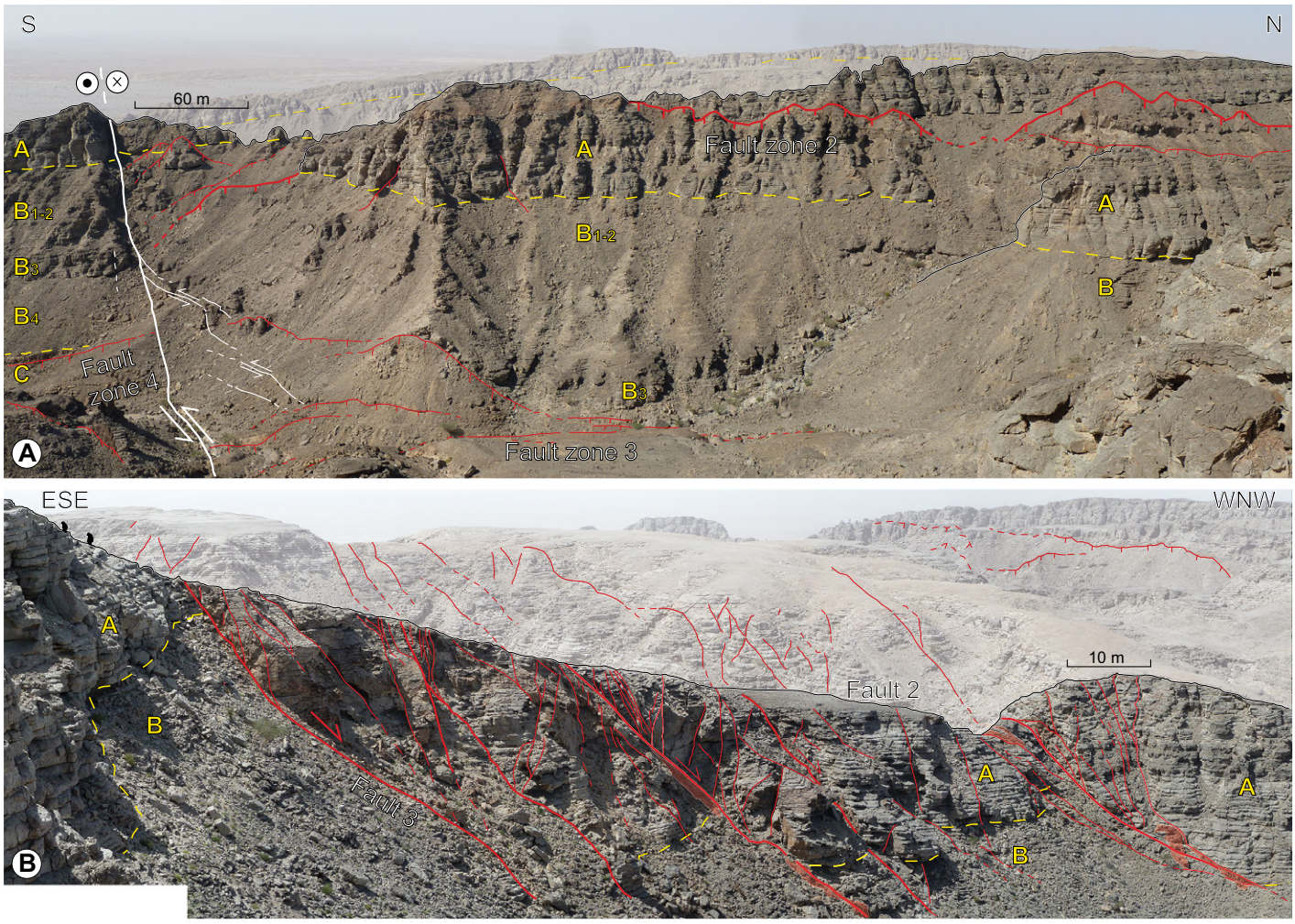

Figure 5. (A) Panoramic view of N-S extensional fault zones abutting NE-SW left-lateral strike-slip fault zone. (B) Structural architecture of the zone of interaction between fault zones 2 and 3 showing fault splaying, and subsidiary synthetic and antithetic faulting.

increasing toward the main slip surfaces (Figs. 8A and 9A). The boundary between brecciated rocks and the adjacent damage zones is transitional and marked by a complex set of fault-parallel veins connected by cross-veins (Fig. 9B). Breccias mostly consist of highly angular fragments forming a "jigsaw" texture, with clast size broadly ranging from a few millimeters to ~1 m. Most breccias show limited evidences of multiple fracturing episodes. In a few cases, they are sheared and overprinted by slip surfaces. The fracture mesh is always dilational and sealed with a brown to whitish calcite cement rather than comminuted matrix (Figs. 9B and 9C). The amount of cement can volumetrically exceed that of the fragments.

The thickness and spatial distribution of breccia bodies in the study area are shown in Figure 10. Thicker and more-developed breccias occur at strike-slip fault releasing jogs and extensional quadrants, at the intersection zones between strike-slip and extensional fault zones (e.g., north termination of fault zone 1), and at the tip regions of extensional fault zones (e.g., north termination of fault zone 2). Brecciated rocks are locally reopened by decimeter- to meter-thick arrays of fractures infilled by euhedral, centimeter- to decimeter-thick, oil-bearing calcite crystals and aggregates (fault infillings; Fig. 9D).

Fault Zone Interaction and Vein Patterns

The areas of interaction between extensional and strike-slip fault zones are characterized by a general increase in structural complexity (Fig. 4). For example, extensional fault zones 1 and 3 widen into minor splay faults approaching the major NE-SW strike-slip fault zones (Figs. 4 and 11A–11B).

In the northern intersection area (Fig. 11A), subsidiary faults and veins are mostly localized in the footwall of fault zone 1. Splay fault zones have displacements <1 m and show extensional to oblique-slip kinematics. Vein density increases within the intersection zones (Fig. 11C). In these intersection zones, the general approximately N-S vein trend associated with fault zone 1 becomes near-parallel to the NE-SW, left-lateral strike-slip fault zone. Moreover, in the intersection zone, an additional set of NNW-SSE to NW-SE veins is also present. Crosscutting relationships among N-S, NE-SW, and NNW-SSE veins do not show a systematic relative chronology, as these vein sets are mutually crosscutting.

To the east of the intersection zone of fault zone 1, the NE-SW left-lateral strike-slip fault zone segment overlaps with an E-W segment, thus forming an ~5-m-wide dilational jog (Figs. 4 and 11A). In this dilational jog, veins strike mainly NE-SW and, approaching the principal slip surface, are connected by closely spaced, nonsystematic veins sets (Fig. 11D), thus resulting in a protobreccia texture (Figs. 8E and 11E).

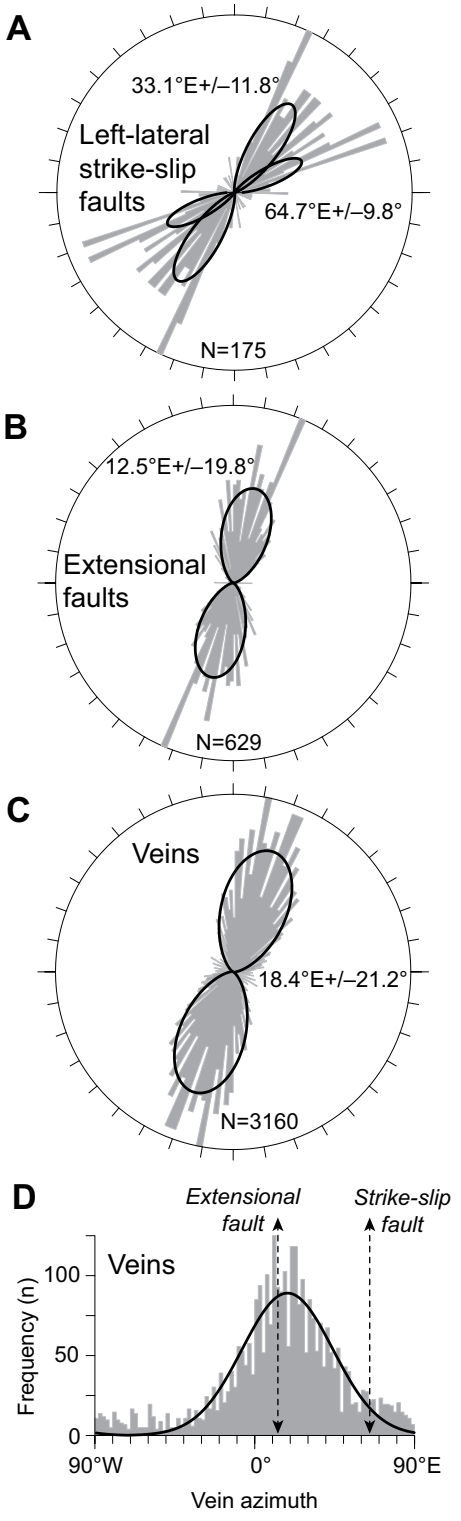

Figure 6. Cumulative statistical analysis of the azimuth of (A) left-lateral strike-slip fault zones, (B) extensional fault zones, and (C) veins. (D) Graph showing the frequency (%) vs. azimuth of veins.

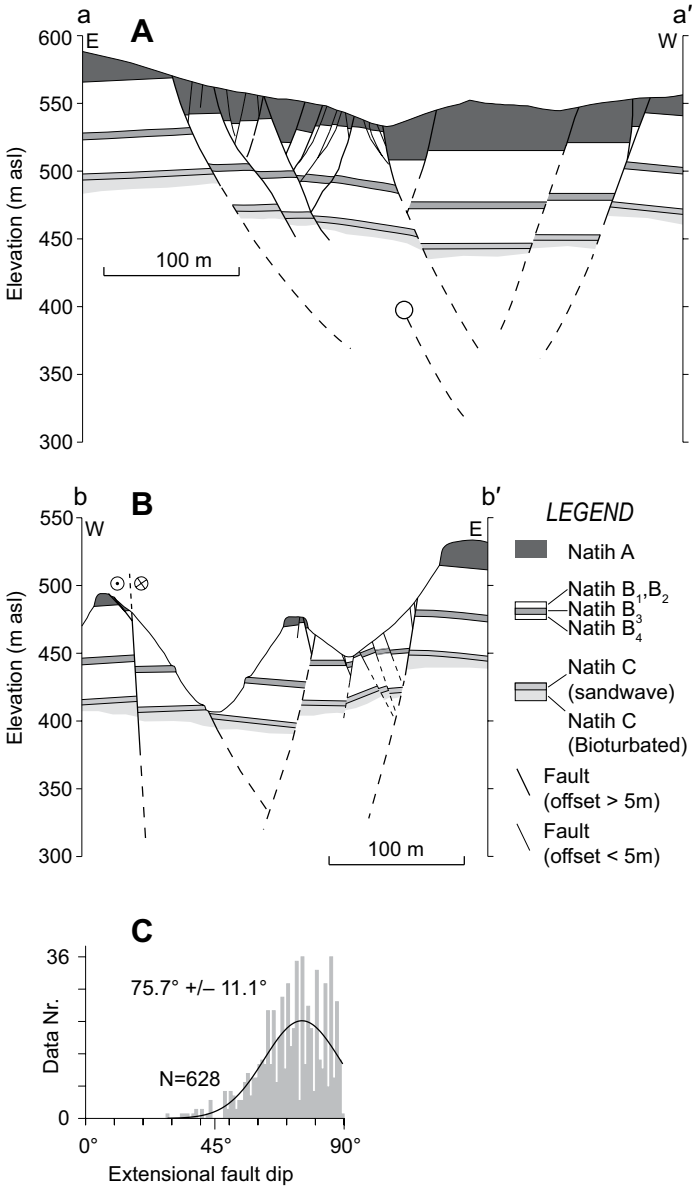

Figure 7. (A, B) Geological E-W–oriented cross sections showing the architecture of N-S extensional fault zones and the absence of significant rollover structures (m asl—m above sea level). See Figure 4 for location. (C) Gaussian distribution statistics of extensional fault zone dip, showing a major peak at 75.7° ± 11.1°.

Extensional Fault Zone Attributes and Displacement Profiles

The trace length (L) of extensional fault zones, measured in map view, is plotted against the maximum fault displacement (D_{max}) in Figure 12A. The data exhibit a slight scatter in length over almost three orders of magnitude, showing a steep best-fit slope. Maximum damage zone thicknesses (T_{DZ}) of both extensional and strike-slip fault zones are plotted against fault displacement, showing a positive correlation. In particular, data from extensional fault zones are satisfactory fit by ~D_{max} = T_{DZ} line, while those from strike-slip fault zones cluster around a steep best-fit line if the two low-displacement outliers are ignored (Fig. 12B). Maximum fault-core thickness (T_{FC}) data, which typically include the dilation-related breccia bodies, show increasing values with increasing displacement, despite the significant scattering evident when data are visualized in linear space (Fig. 12C).

Geological Society of America Bulletin, published online on 10 February 2016 as doi:10.1130/B31317.1

Figure 8. Main features of fault zones exposed in Jabal Qusaybah. (A) Example of fault core surrounded by footwall (FW) and hanging-wall (HW) damage zones. A meter-thick breccia body is interposed between fault core and the hanging-wall damage zone; site J in Figure 4. (B) Example of downdip slickenlines developed in the synthetic shear surface of an extensional fault zone at site J in Figure 4. (C) Multiple slickenlines indicating progressive transtensional reactivation in a steeply dipping extensional fault zone; site D in Figure 4. (D) Example of fault-parallel veins developed in the hanging-wall damage zone of an extensional fault zone; site F in Figure 4. (E) Example of oblique vein pattern associated with a strike-slip fault zone; site B in Figure 4. See Figure 11D for a line drawing of this image.

Along-strike displacement profiles for extensional fault zones 1–5, shown in Figure 4, are shown in Figure 13A. The length of these fault zones ranges from 299 m to 865 m, and the maximum net slip ranges between 8 m and 60 m (Table 1). The maximum net slip in fault zones 2 and 5, which do not abut the strike-slip fault zones, occurs near the center of the fault traces, and displacement tapers off gradually toward the fault tips. In contrast, the maximum net slip of extensional fault zones that abut strike-slip faults occurs close to the intersection zones, with the exception of fault zone 3, which shows maximum displacement in its central sector (Fig. 13A). This results in strongly asymmetric slip distributions with flat-topped displacement profiles for the extensional faults as they approach the strike-slip fault zones. The black

Geological Society of America Bulletin, published online on 10 February 2016 as doi:10.1130/B31317.1

Figure 9. Main features of brecciated rocks. (A) Sharp transition between damage zone and dilation breccias; site D in Figure 4. (B) Complex vein network marking the transition between damage zone and breccias; site D in Figure 4. (C) Jigsaw fit texture of breccias with angular carbonate fragments (in gray) and calcite-filled fracture meshes (in brown); site D in Figure 4. (D) Euhedral, centimeter- to decimeter-thick calcite crystals developed within the fault core of an extensional fault zone; site I in Figure 4.

line in Figure 13A represents the cumulative displacement of all extensional faults measured in 250-m-spaced, E-W transects and projected along the N-S transect. The maximum cumulative displacement values occur in the crestal sector of the Jabal Qusaybah anticline and are confined to the area between the two major strike-slip fault zones. A subsidiary peak is located in the southern fold limb. The cumulative displacement decreases, roughly symmetrically, from the peak value to the strike-slip fault zones, where it abruptly drops to lower values outside the area of the fault-bounded compartment, and tapers to zero in both northern and southern fold limbs.

The displacement gradient (sensu Walsh and Watterson, 1988) has been calculated for the five fault zones, both in the central sectors and at fault zone tips (Fig. 13B; Table 1). Fault zone 5 has the highest values in the central sector and the lowest values near the fault zone tip (Fig. 13B). Fault zones 3 and 4, which abut against the southern strike-slip fault zone, has a maximum displacement gradient near the center. Fault zone 1 has the highest value at the tip. Fault zone 2 has two maximum displacement gradients at the southern tip and at the central sector. Fault zone length, displacement, D_{max}/L ratios, and displacement gradients at the tip and at the center of faults 1–5 are summarized in Table 1.

VEIN PETROGRAPHY, ISOTOPE GEOCHEMISTRY, AND MICROTHERMOMETRY DATA

Vein infillings in fault damage zones were classified into groups 1, 2, and 3 following the classification of Storti et al. (2015). Group 1 veins are local veins that are dispersed in the limestones, and these were not included in this study since they are linked to burial and early E-W extension (see Mozafari et al., 2015 for more details). Group 2 includes older calcite generations, widely precipitated in fracture meshes of brecciated rocks and fault infillings along strike-slip fault zones and strike-slip tip regions

Geological Society of America Bulletin, published online on 10 February 2016 as doi:10.1130/B31317.1

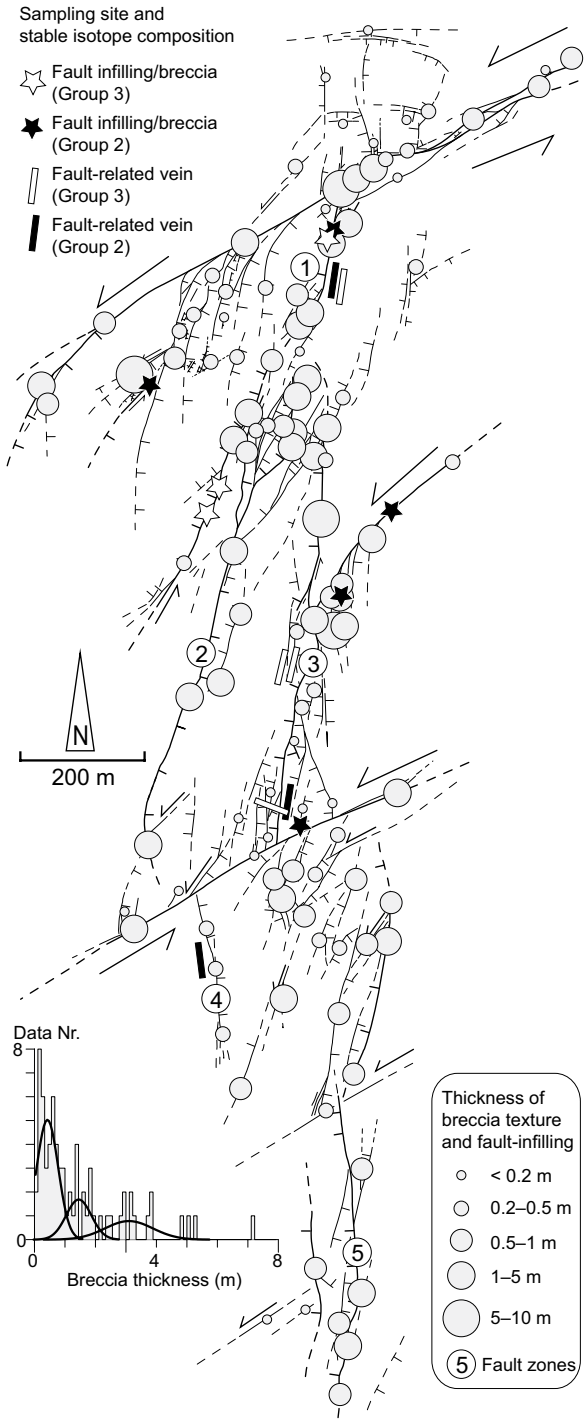

Figure 10. Spatial distribution and thickness of breccias and calcite fault infillings. Sampling sites and classification of selected samples are also indicated. Higher volumes of breccias are localized at fault tips and fault intersection areas.

and, subordinately, in approximately N-S veins within the extensional fault zones (Figs. 10 and 14A). Group 3 includes calcite generations that overprint the older ones and occur mostly within approximately N-S veins, fracture meshes of brecciated rocks, and fault-core infillings of extensional fault zones (Figs. 10 and 14B).

Group 2 cement infillings are typically characterized by slightly ferroan to ferroan blocky crystals with a random orientation. Within this group, early crystals are characterized by a milky white to pale-yellow color, and intense crystal deformation twinning with undulose extinction (Fig. 14A). Late crystals have black/gray or translucent white colors, little to no cleavage twinning, and pervasive brown alteration in hand specimens. The $\delta^{18}O$ values of this group of calcite vary between –11.2‰ and –2.3‰ VPDB (~+19‰ and +29‰ VSMOW; Fig. 14C) and are remarkably different from the original stable isotope values of the Natih Formation marine carbonates (–3.0‰ and –0.5‰ VPDB; Immenhauser et al., 2000). In contrast to the broad range of $\delta^{18}O$ values, the $\delta^{13}C$ values display a relatively narrow range of +1.9‰ to +3.2‰ VPDB (Fig. 14C), which is within the range of the original stable isotope values of the Natih Formation marine carbonates (–1.0‰ and +3.5‰ VPDB; Immenhauser et al., 2000). Fluid inclusions in group 2 calcite are biphase at room temperature and are characterized by a wide range of homogenization temperatures, varying between 65 °C and 97 °C (Fig. 14D).

Group 3 cements include calcite crystals characterized by lower Fe content and white to translucent colors (Fig. 14B). Bladed to scalenohedral crystals in fault-core infillings, with size up to 30 cm, are generally elongated orthogonal to the fracture walls. The $\delta^{18}O$ compositions demonstrate relatively less-depleted values ranging between –3.8‰ and +1.2‰ VPDB (~+27‰ to +32‰ VSMOW). The $\delta^{13}C$ composition varies between +0.6‰ and +6.6‰ VPDB (Fig. 14C), showing higher values than the Natih host rocks and group 2 veins. This group of veins contains aqueous monophase inclusions at room temperature (Fig. 14D). Figure 14E shows calculated parent fluid composition for the two cement groups obtained by combining the information from stable isotope scatterplot (Fig. 14C) and fluid inclusion microthermometry data (Fig. 14D).

DISCUSSION

Origin of Dilation Breccias and Paleofluid Flow

The presence of angular fragments with jigsaw-fit texture, and the absence of an intrafragmental matrix (Figs. 9B and 9C) support the interpretation that the brecciated rock bodies documented in the study area consist of dilation breccias (Woodcock et al., 2007), i.e., fragmented rocks in which there has been a net volume increase during formation (Tarasewicz et al., 2005, and references therein). The more-evolved brecciated rocks documented in this study, as thick as ~7 m and in which the volume of precipitated calcite cement exceeds that of the limestone fragments (Fig. 9A), can be classified as chaotic breccias (Mort and Woodcock, 2008). The sharp boundaries of angular fragments (Figs. 9B and 9C) indicate that metasomatic replacement of breccia fragments by calcite cements was not likely the primary process responsible for the observed fabric. The crystalline textures of calcite infillings in most fracture meshes of brecciated rocks, combined with the very limited

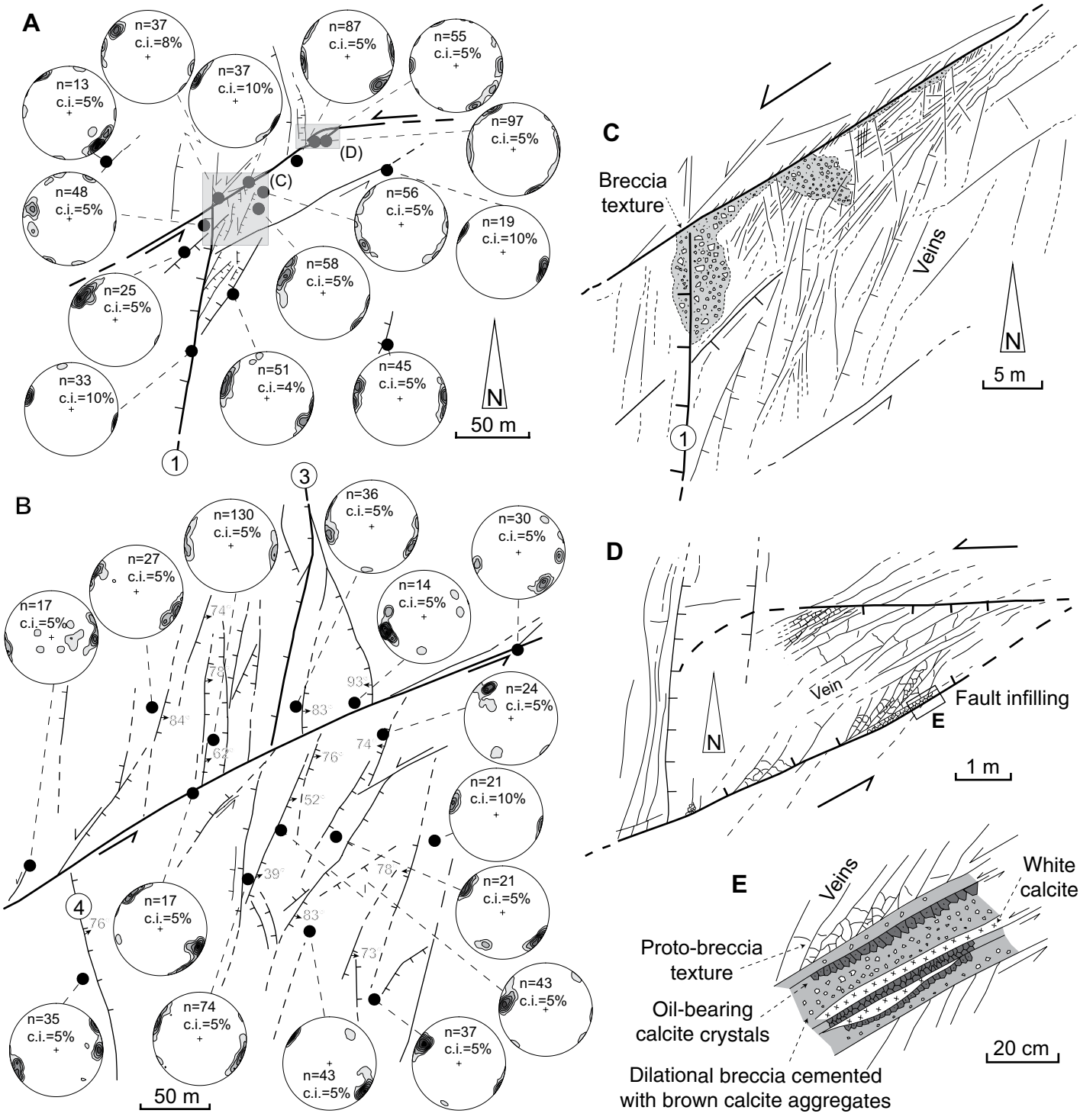

Figure 11. Structural patterns at fault intersection areas between northern and southern strike-slip fault zones and (A) extensional fault zone 1, and (B) extensional fault zones 3 and 4, respectively. Pole to veins in stereonets (Schmidt net, lower hemisphere). (C) Detail of A showing fault splaying, veining, and local brecciation at intersection areas. (D) Detail of A showing NNE-SSW–oriented veins associated with NE-SW left-lateral strike-slip fault zones; see Figure 8E for the corresponding photograph. (E) Detail of D showing breccias and centimeter-thick calcite crystals

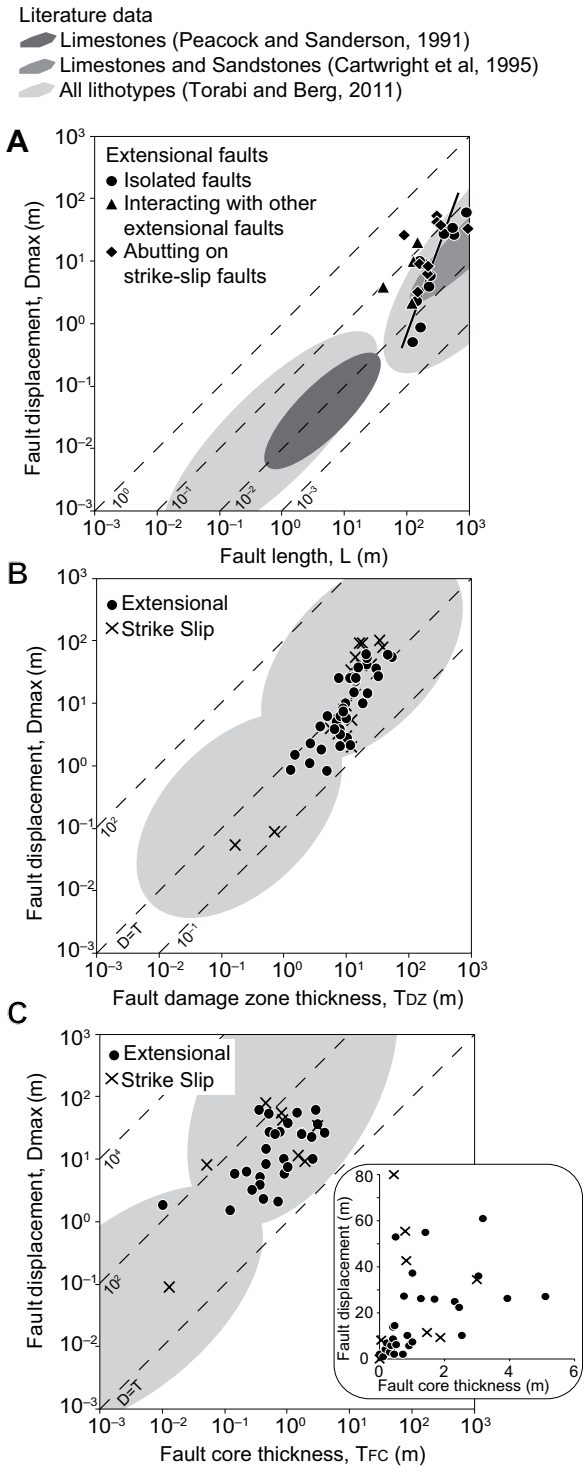

Figure 12. Extensional and strike-slip fault zone attributes plotted in log-log spaces. (A) Fault zone length vs. fault displacement. (B) Fault damage zone thickness vs. fault displacement. (C) Fault core thickness vs. fault displacement. The inset shows fault core (and breccia) thickness vs. fault displacement in linear space. For comparison, the gray areas in the background represent fault data compilations for extensional faults in limestones and other lithologies (Cartwright et al., 1995; Torabi and Berg, 2011).

refracturing of breccias (Fig. 9C), suggest that fragmentation and dilation along fault zones happened concurrently and very rapidly during single episodes of brecciation (Woodcock et al., 2007). The absence of fibrous fabrics in calcite cements between the breccia fragments suggests that brecciation may have occurred at elevated strain rates, possibly during seismic events (Sibson, 1996; Woodcock et al., 2007), thus causing a pressure drop and promoting cement precipitation. Factors that may have promoted the extensive dilation and development of breccias and fault-core infillings in the Jabal Qusaybah anticline include: (1) the transtensional kinematics of the strike-slip fault zones, particularly at fault zone tip regions (Fig. 4), further enhanced by axial bulging during folding (Storti et al., 2015); (2) low confining pressure and low differential stress along fault tips (extensional quadrants) and releasing (dilational) fault jogs (Woodcock et al., 2007); and (3) a potential top seal provided by the shales of the Fiqa Formation, which would aid maintenance of high fluid pressure in the underlying Natih carbonates. This is also supported by the presence of centimeter- to decimeter-thick bedding-parallel veins in the upper part of Natih member A (Storti et al., 2015), which implies involvement of pore pressure locally exceeding the overburden stress.

The spatial distribution of major breccia volumes at tip regions, fault zone oversteps, and intersections (Fig. 10), and the presence of higher fracture frequencies and multiple vein sets in those areas (Fig. 11C), implies that the structural position, and not fault displacement, is the dominant parameter that controlled the location of the more dilatants areas within the Jabal Qusaybah anticline. This inference is also supported by the broad scattering in fault core and breccia thickness-displacement data in a linear-linear plot (inset in Fig. 12C).

The spatial distribution of group 2 and 3 calcite crystals forming breccia cements (Fig. 10), the different vein petrography (Figs. 14A and 14B), their isotopic signatures, and microthermometric data (Figs. 14C and 14D) support the inference of two chronologically distinct episodes of brecciation and cementation during folding. The isotopic composition and fluid inclusion microthermometry data indicate that group 2 fault infillings and cement breccia textures, developed along NE-SW strike-slip fault zones and N-S splay fault zones, precipitated at temperatures greater than 70 °C. It was associated with a slightly enriched parent fluid (+3‰ to +8‰ VSMOW; Fig. 14E) and occurred at ~3–4 km depths, with the assumption of a classical geothermal gradient for foreland thrust belts (e.g., 20 °C/km). The broad variability in oxygen isotope composition within group 2 reflects the existence of several subgenerations of vein infills (Mozafari et al., 2015) that are not described in detail in the present paper. Conversely, monophase inclusions in group 3 fault infillings and cement breccia textures precipitated along N-S extensional fault zones are interpreted as evidence for trapping temperatures below 50 °C, indicative of less than ~2 km depth with the same assumption as for group 2 veins. These shallow depths for the second-stage breccia texture development are consistent with late-stage extensional faulting during fold amplification and exhumation (cf. Storti et al., 2015). Due to the uncertainty in trapping temperature estimation, the parent fluid composition associated with group 3 calcite is not well

Geological Society of America Bulletin, published online on 10 February 2016 as doi:10.1130/B31317.1

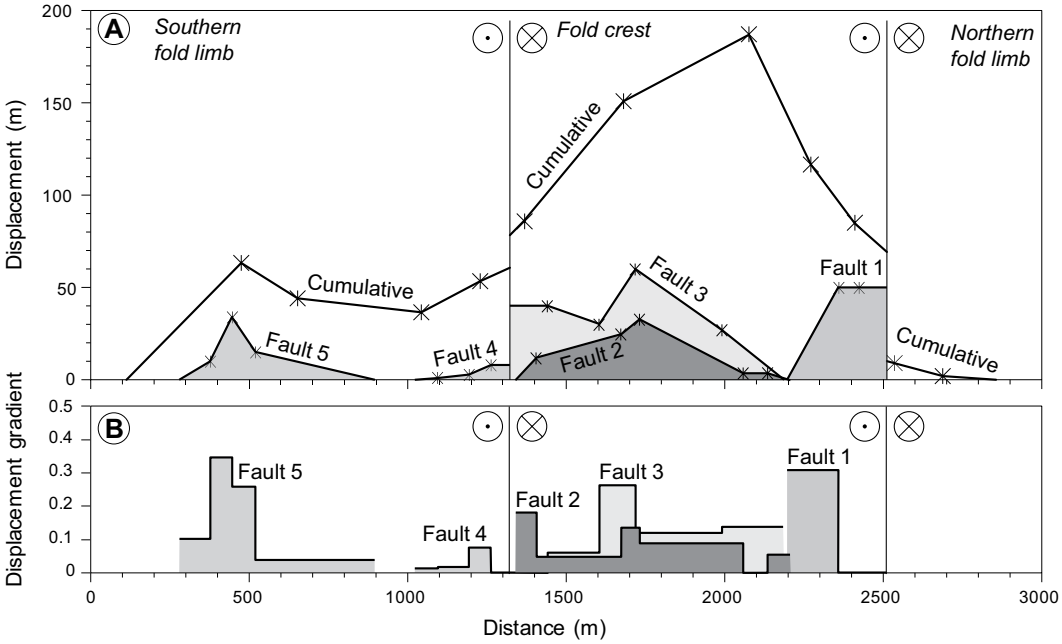

Figure 13. (A) Displacement-distribution profiles along a N-S transect for five selected extensional fault zones. The cumulative net slip values, obtained from all mapped fault zones, are also projected. (B) Displacement gradients calculated in the tip regions and central sectors of selected extensional fault zones.

constrained, but it might range from slightly depleted to slightly enriched parent fluid (–2‰ to +6‰ VSMOW; Fig. 14E).

Extensional Fault Zone Anatomy

For given displacement values, extensional fault zones in the Jabal Qusaybah anticline are significantly shorter than values commonly observed in extensional tectonic settings worldwide (Fig. 15). The aforementioned fault zones are geometrically comparable to the laterally restricted extensional fault zones in the Timor Sea, characterized by displacement values of 20–50 m and trace lengths <1 km (Nicol et al., 1996). The anomalous lengths of the studied fault zones are also indicated by the steep best-fit line of displacement-length scaling data, which significantly deviates from the inclination of best-fit lines obtained from reported cumulative data sets (Fig. 12A).The D_{max}/L ratios of the studied fault zones, ranging between 0.027 and 0.15 (Table 1), are consistently and significantly higher than values reported for extensional fault zones with comparable displacements (Dawers et al., 1993). Furthermore, the isolated extensional fault zones described in the present work have cuspate-shaped and peaked displacement profiles rather than the more typical elliptical shapes, with higher displacement gradients in the central sectors (Table 1; faults 2, 3, and 5 in Fig. 13A). Geometrical parameters collectively suggest that, during their synfolding activity, extensional fault zones in Jabal Qusaybah accumulated part of their displacement without significant lateral propagation.

Three main factors may have contributed to produce the observed geometrical properties of the N-S extensional fault zones: (1) the presence of preexisting NE-SW, left-lateral strike-slip fault zones (Fig. 4), which provided vertical mechanical barriers that inhibited their lateral propagation (Fig. 13); (2) fault tip hardening due to resealing processes (Woodcock et al., 2007), induced by concurrent rapid dilation and cement precipitation in meter-thick dilation breccias (Fig. 10), which made the breccias stronger that the intact rock and inhibited further lateral fault propagation; and (3) diffuse splay faulting and veining at (i) fault tip regions (Fig. 4), and (ii) intersection areas between strike-slip and extensional fault zones (Fig. 11), which may have contributed to displacement tapering toward fault terminations (see numerical simulation in Bürgmann et al., 1994).

Conceptual Growth Model for Laterally Restricted Extensional Fault Zones

Based on field observations, geometrical attributes of extensional fault zones, and geochemistry of brecciated rocks and veins, the following evolutionary model composed of two largely overlapping, concurrent processes is proposed for the Jabal Qusaybah anticline. Process 1 is characterized by dominant NE-SW strike-slip faulting and subsidiary N-S splay faulting, brecciation, and cementation with hot fluids (65–100 °C) at a depth of 3–4 km during the early growth history of the anticline (Fig. 16A). Isolated N-S extensional fault zones were still embryonic and accommodated displacement by lateral propagation in layered Natih carbonates within the fault-bounded compartments. Process 2 is younger and occurred at depths <2 km during late-stage fold axial bulging and possible salt migration (Storti et al., 2015), at which time the propagation of N-S transverse extensional fault zones was enhanced (Fig. 16B). In this structural framework, strike-slip fault segments limited the horizontal component of such propagation, thus promoting vertical growth and associated displacement accumulation that increased displacement gradients near the center of the faults (Fig. 16C). Downward propagation of the fault tip line would be expected. Breccia development and calcite precipitation along N-S extensional fault zones would further decrease

TABLE 1. GEOMETRICAL ATTRIBUTES OF SELECTED EXTENSIONAL FAULTS AND DISPLACEMENT GRADIENTS CALCULATED NEAR FAULT TIPS (ISOLATED FAULTS) AND IN THE CENTRAL PARTS

Fault type	Fault no.	L (m)	D_{max} (m)	Displacement gradients		D_{max}/L
				Tip	Center	
Isolated	2	865	33	0.055	0.136	0.038
	5	615	34	0.040	0.348	0.055
Abutting	4	299	8	0.014	0.076	0.026
	1	315	50	0.309	0.000	0.159
	3	863	60	0.121	0.264	0.070

Note: L—horizontal fault length; D_{max}—maximum fault displacement.

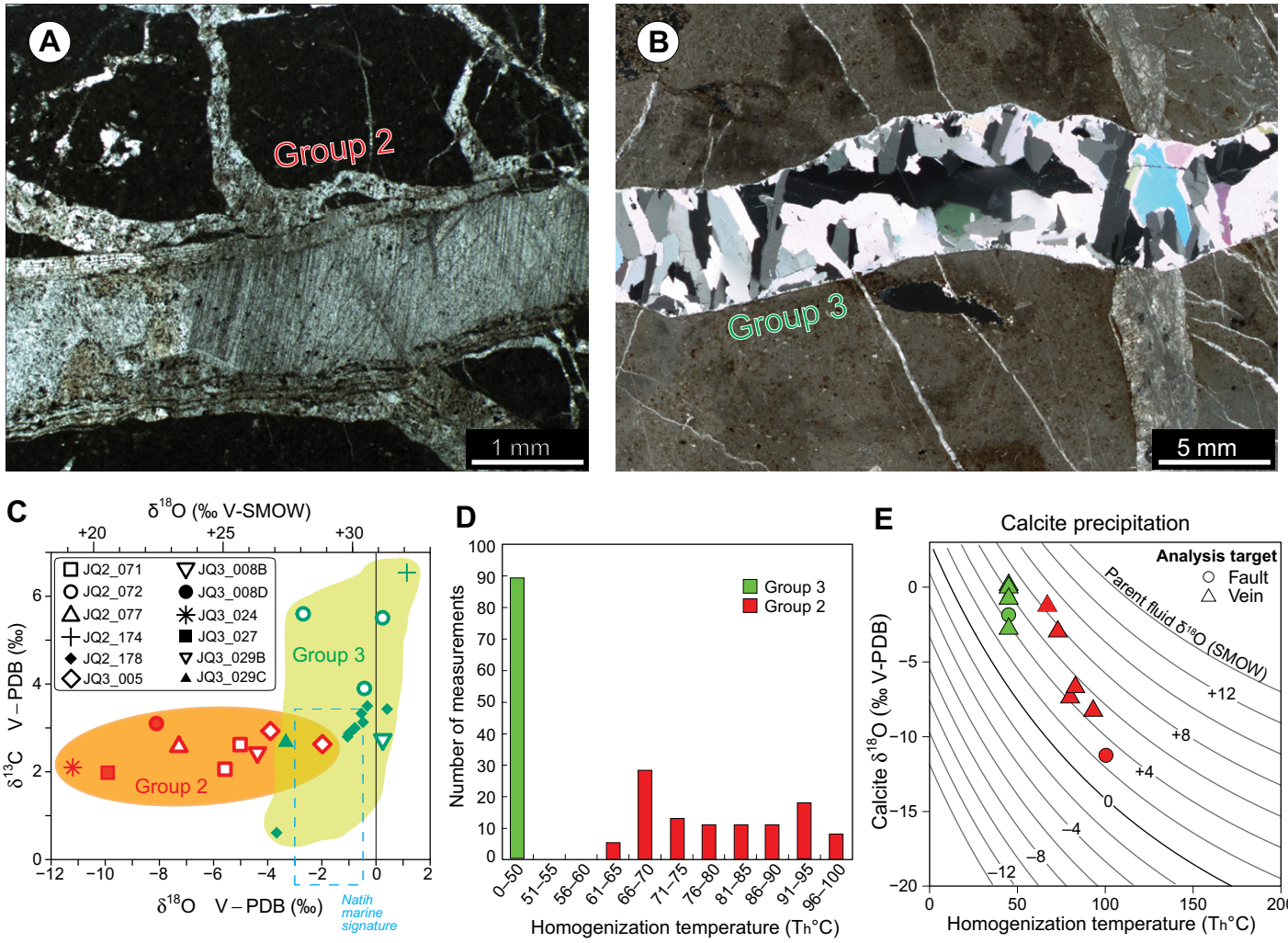

Figure 14. Main petrographic features of (A) group 2 and (B) group 3 calcite veins. (C) Stable carbon-oxygen isotopic signature of group 2 and 3 calcite veins and fault infillings. (D) Histograms showing the distribution of homogenization temperatures (T_h) in group 2 and 3 calcite veins, with bin width 5 °C. (E) Oxygen isotope fractionation during equilibrium precipitation: calcite (vertical axis) and fluid (curves) composition as a function of temperature. Red and green symbols indicate the group 2 and 3 calcite cement (see text for details). V-PDB—Vienna Peedee belemnite; V-SMOW—Vienna standard mean ocean water.

their outward propagation due to resealing hardening processes in sectors of enhanced dilatancy, i.e., at fault tip regions and fault intersections.

CONCLUSIONS

The Jabal Qusaybah anticline, at the southern tip of the Oman Mountains, is characterized by well-developed transverse extensional fault zones that formed during folding, concurrent with the activity of obliquely trending, left-lateral strike-slip fault zones. These extensional fault zones accommodated significant amounts of fold-parallel dilation associated with longitudinal axial bulging. Interaction between outer-arc (<2 km depth) extensional and strike-slip faulting (at 3–4 km depth), and anticlinal folding produced peculiar geometrical fault patterns, anomalous

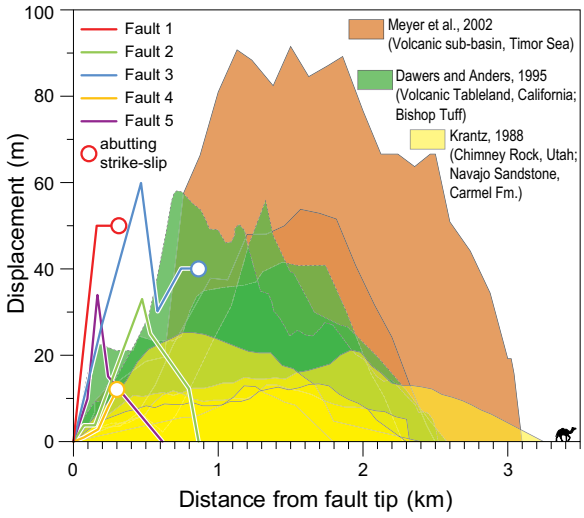

Figure 15. Comparison between displacement-distance profiles of the studied extensional fault zones in Jabal Qusaybah, and extensional fault zones with similar displacement developed in other tectonic and stratigraphic settings.

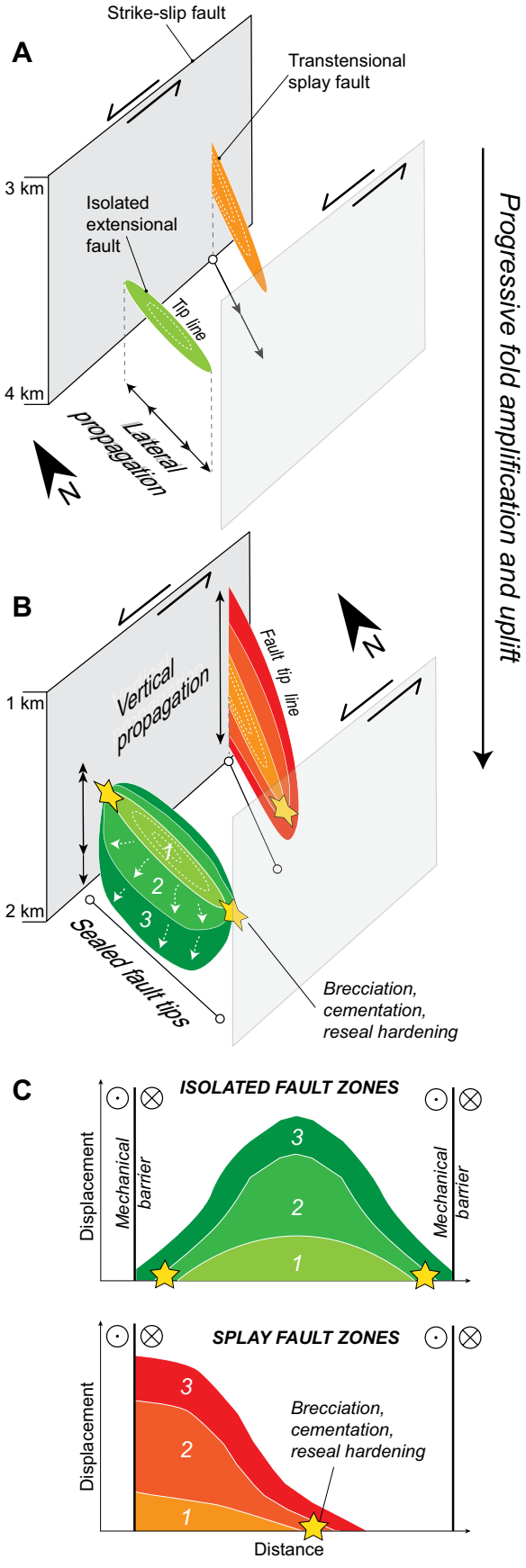

Figure 16. (A–B) Evolutionary model showing the development of extensional fault zones within a strike-slip–bounded compartment during progressive folding and uplift. Extensional fault zones propagate laterally until they reach the vertical mechanical barrier provided by strike-slip fault zones. Dilation breccias and rapid cementation further strengthen the fault tip regions, thus inhibiting lateral propagation and promoting vertical fault propagation during late extensional faulting. (C) Schematic diagrams representing the displacement-distance profiles of a splay fault zone and an isolated extensional fault zone during the two main stages. See text for details.

fault attributes, and calcite cement distributions characterized by significant volumes of dilation breccias and fault-core infillings. The growth of the N-S extensional fault zones was influenced by two main factors: (1) the presence of subvertical mechanical barriers represented by strike-slip fault zones, which hindered their lateral propagation, and (2) development of significant volumes of dilation breccias and precipitation of abundant calcite infillings in fault tip regions and areas of fault intersection, which may have increased the frictional strength of fault strands by reseal-hardening processes.

The evolutionary model proposed for folding-related faulting during the growth of the Jabal Qusaybah anticline exemplifies two different major fault kinematics (strike-slip and extension), separated in origin and position (relatively deep and relatively shallow, respectively), but kinematically linked in space and time. The strike-slip and extensional strain domains were initiated concurrently and progressively interacted, thereby becoming interrelated as the anticline grew. This model has important implications for growth models of interacting fault segments and indicates that areas of enhanced fault connectivity can be localized in the central sectors of anticlines similar to Jabal Qusaybah, in particular, at fault tip regions and fault intersections. Thus, in this case, structural position is the dominant parameter controlling the location of the more dilatant areas. The peculiar growth history of the studied extensional fault zones is expected to have also influenced the evolution of fracture patterns within fault damage zones, thus impacting fluid-flow predictions in carbonate reservoirs developed in foreland fold-and-thrust belts in analogous structures (salt-cored anticlines compartmentalized by fault zones striking at a high angle to the fold hinge).

ACKNOWLEDGMENTS

This work is part of a joint research project between Parma and KU Leuven universities, funded by Shell Global Solutions International. We are grateful to Shell for releasing this material for publication. We are also grateful to L. Barchi, A. Comelli, and H. Nijs for support with thin section preparation. We warmly thank F. Mondino (formerly at Shell) for the enthusiastic support she gave to the early stages of this project. The manuscript strongly benefited from discussions with L. Bazalgette, A. Koopman, and P. Richard. A. Koopman is also thanked for his accurate revision of an early manuscript version. Associate Editor E. Tavarnelli, and the two reviewers F. Agosta and F. Calamita, are kindly thanked for their constructive criticism and comments.

REFERENCES CITED

Al-Kindi, M.H., 2006, Structural evolution and fracture pattern of Salakh Arch [Ph.D. thesis]: Leeds, UK, University of of Leeds.

Al-Kindi, M.H., and Richard, P.D., 2014, The main structural styles of the hydrocarbon reservoirs in Oman, *in*

Rollinson, H.R., Searle, M.P., Abbasi, I.A., Al-Lazki, A.I., and Al Kindi, M.H., eds., Tectonic Evolution of the Oman Mountains: Geological Society of London of Special Publication 392, p. 409–445, doi:10.1144/SP392.20.

Arndt, M., Virgo, S., Cox, S.F., and Urai, J.L., 2014, Changes in fluid pathways in a calcite vein mesh (Natih Formation, Oman Mountains): Insights from stable isotopes: Geofluids, v. 14, p. 391–418, doi:10.1111/gfl.12083.

Balsamo, F., and Storti, F., 2010, Grain size and permeability evolution of soft-sediment extensional sub-seismic and seismic fault zones in high-porosity sediments from the Crotone basin, Southern Apennines, Italy: Marine and Petroleum Geology, v. 27, p. 822–837, doi:10.1016/j.marpetgeo.2009.10.016.

Bürgmann, R., Pollard, D.D., and Martel, S.J., 1994, Slip distributions on faults: Effects of stress gradients, inelastic deformation, heterogeneous host-rock stiffness, and fault interaction: Journal of Structural Geology, v. 16, p. 1675–1690, doi:10.1016/0191-8141(94)90134-1.

Caine, J.S., Evans, J.P., and Forster, C.B., 1996, Fault zone architecture and permeability structure: Geology, v. 24, p. 1025–1028, doi:10.1130/0091-7613(1996)024<1025:FZAAPS>2.3.CO;2.

Cartwright, J.A., Trudgill, B.D., and Mansfield, C.S., 1995, Fault growth by segment linkage: An explanation for scatter in maximum displacement and trace length data from the Canyonlands grabens of SE Utah: Journal of Structural Geology, v. 17, p. 1319–1326, doi:10.1016/0191-8141(95)00033-A.

Childs, C., Nicol, A., Walsh, J.J., and Watterson, J., 2003, The growth and propagation of synsedimentary faults: Journal of Structural Geology, v. 25, p. 633–648, doi:10.1016/S0191-8141(02)00054-8.

Cowie, P.A., and Scholz, C.H., 1992, Displacement-length scaling relationships for faults: Data synthesis and discussion: Journal of Structural Geology, v. 14, p. 1149–1156, doi:10.1016/0191-8141(92)90066-6.

Dawers, N.H., and M.H. Anders, 1995, Displacement-length scaling and fault linkage: Journal of Structural Geology, v. 17, p. 607–614.

Dawers, N.H., Anders, M.H., and Scholz, C.H., 1993, Growth of normal faults: Displacement-length scaling: Geology, v. 21, p. 1107–1110, doi: 10.1130/0091-7613(1993)021<1107.

Dickson, J.A.D., 1966, Carbonate identification and genesis as revealed by staining: Journal of Sedimentary Research, v. 36, p. 491–505, doi:10.1306/74D714F6-2B21-11D7-8648000102C1865D.

Filbrandt, J., Al-Dhahab, S., Al Habsy, A., Harris, K., Keating, J., Al Mahruqi, S., Ozkaya, S.I., Richard, P., and Robertson, T., 2006, Kinematic interpretation and structural evolution of North Oman, Block 6, since the Late Cretaceous and implications for timing of hydrocarbon migration into Cretaceous reservoirs: GeoArabia, v. 11, p. 97–140.

Fossen, H., and Hesthammer, J., 1997, Geometric analysis and scaling relations of deformation bands in porous sandstone: Journal of Structural Geology, v. 19, p. 1479–1493, doi:10.1016/S0191-8141(97)00075-8.

Friedman, I., and O'Neil, J.R., 1977, Compilation of stable isotope fractionation factors of geochemical interest, *in* Fleisher, M., ed., Data of Geochemistry (6th ed.): U.S. Geological Survey Professional Paper 440-KK, 117 p.

Goldstein, R.H., and Reynolds, T.J., 1994, Systematics of Fluid Inclusions in Diagenetic Minerals: Society for Sedimentary Geology (SEPM) Short Course 31, 199 p., doi:10.2110/scn.94.31.

Hanna, S.S., and Smewing, J.D., 1996, The stratigraphy and structure of the Madamar-Salakh-Qusaybah range and Natih-Fahud area in the Oman Mountains: Journal of Science and Technology, Sultan Qaboos University, Oman, v. 1, p. 1–19.

Homewood, P.W., Razin, P., Grélaud, C., Droste, H., Vahrenkamp, V., Mettraux, M., and Mattner, J., 2008, Outcrop sedimentology of the Natih Formation, northern Oman: A field guide to selected outcrops in the Adam Foothills and Al Jabal al Akhdar areas: GeoArabia, v. 13, p. 39–120.

Immenhauser, A., Creusen, A., Esteban, M., and Vonhof, H.B., 2000, Recognition and interpretation of polygenic discontinuity surfaces in the Middle Cretaceous Shuaiba, Nahr Umr, and Natih Formations of northern Oman: GeoArabia, v. 5, no. 2, p. 299–322.

Kim, Y.-S., and Sanderson, D.J., 2005, The relationship between displacement and length of faults: A review: Earth-Science Reviews, v. 68, p. 317–334, doi:10.1016/j.earscirev.2004.06.003.

Krantz, R.W., 1988, Multiple fault sets and three-dimensional strain: theory and application: Journal of Structural Geology, v. 10, p. 225–238.

Lisle, R.J., 1994, Detection of zones of abnormal strains in structures using Gaussian curvature analysis: American Association of Petroleum Geology Bulletin, v. 78, p. 1811–1819.

Mort, K., and Woodcock, N.H., 2008, Quantifying fault breccia geometry: Dent fault, NW England: Journal of Structural Geology, v. 30, p. 701–709, doi:10.1016/j.jsg.2008.02.005.

Meyer, V., Nicol, A., Childs, C.J., Walsh, J.J., and Watterson, J., 2002, Progressive localization of strain during the evolution of a normal fault population: Journal of Structural Geology, v. 24, p. 1215–1231, doi:10.1016/S0191-8141(01)00104-3.

Mount, V.S., Crawford, R.I.S., and Bergman, S.C., 1998, Regional structural style of the central and southern Oman Mountains: Jebel Akhdar, Saih Hatat, and the northern Ghaba Basin: GeoArabia, v. 3, p. 475–489.

Mozafari, M., Swennen, R., Balsamo, F., Clemenzi, L., Storti, F., El Desouky, H.A., Tueckmantel, C., Solum, J. and Taberner, C., 2015, Paleofluid evolution in fault-damage zones: Evidences from fault-fold interaction events in the Jabal Qusaybah anticline (Adam Foothills, North Oman): Journal of Sedimentary Research, v. 85, no. 12, p. 1525–1551, doi:10.2110/jsr.2015.95.

Nicol, A., Watterson, J., Walsh, J.J., and Childs, C., 1996, The shapes, major axis orientations and displacement patterns of fault surfaces: Journal of Structural Geology, v. 18, p. 235–248, doi:10.1016/S0191-8141(96)80047-2.

Ortega, O.J., Marrett, R.A., and Laubach, S.E., 2006, A scale-independent approach to fracture intensity and average spacing measurement: American Association of Petroleum Geologists Bulletin, v. 90, p. 193–208, doi:10.1306/08250505059.

Peacock, D.C.P., Sanderson, D.J., 1991, Displacement, segment linkage and relay ramps in normal fault zones. Journal of Structural Geoogy, v. 13, p. 721–733.

Richard, P., Bazalgette, L., and Al-Kindi, M., 2014, North Oman fault geometries in outcrops, analogues and subsurface, *in* Rollinson, H.R., Searle, M.P., Abbasi, I.A., Al-Lazki, A.I., and Al Kindi, M.H., eds., Tectonic Evolution of the Oman Mountains: Geological Society of London Special Publication 392, p. 447–460, doi:10.1144/SP392.21.

Roedder, E., 1984, Fluid inclusions, *in* Ribbe, P.H., ed., Reviews in Mineralogy, Volume 12: Washington, D.C., Mineralogical Society of America, 644 p.

Rotevatn, A., and Bastesen, E., 2014, Fault linkage and damage zone architecture in tight carbonate rocks in the Suez Rift (Egypt): Implications for permeability structure along segmented normal faults, *in* Spence, G.H., et al., eds., Advances in the Study of Fractured Reservoirs: Geological Society of London Special Publication 374, p. 79–95, doi:10.1144/SP374.12.

Salvini, F., 2015, Daisy3 Software, The Structural Data Integrated System Analyzer, Version 3_500–5, http://host.uniroma3.it/progetti/fralab/Downloads/Programs (last accessed 22 January 2016).

Scholz, C.H., and Cowie, P.A., 1990, Determination of total strain from faulting using slip measurements: Nature, v. 346, p. 837–839, doi:10.1038/346837a0.

Schultz, R.A., Klimczak, C., Fossen, H., Olson, J.E., Exner, U., Reeves, D.M., and Soliva, R., 2013, Statistical tests of scaling relationships for geologic structures: Journal of Structural Geology, v. 48, p. 85–94, doi:10.1016/j.jsg.2012.12.005.

Sibson, R.H., 1996, Structural permeability of fluid-driven fault-fracture meshes: Journal of Structural Geology, v. 18, p. 1031–1042, doi:10.1016/0191-8141(96)00032-6.

Soliva, R., and Benedicto, A., 2005, Geometry, scaling relations and spacing of vertically restricted normal faults: Journal of Structural Geology, v. 27, p. 317–325, doi:10.1016/j.jsg.2004.08.010.

Soliva, R., Schultz, R.A., and Benedicto, A., 2005, Three-dimensional displacement-length scaling and maximum dimension of normal faults in layered rocks: Geophysical Research Letters, v. 32, p. L16302, doi:10.1029/2005GL023007.

Storti, F., Rossetti, F., Läufer, A.L., and Salvini, F., 2006, Consistent kinematic architecture in the damage zones of intraplate strike-slip fault systems in North Victoria Land, Antarctica, and implications for fault zone evolution: Journal of Structural Geology, v. 28, p. 50–63, doi:10.1016/j.jsg.2005.09.004.

Storti, F., Balsamo, F., Clemenzi, L., Mozafari, M., Al-Kindy, M.H.N., Solum, J., Swennen, R., Taberner, C., and Tueckmantel, C., 2015, Complex fault-fold interactions during the growth of the Jabal Qusaybah inversion anticline at western tip of the Salakh Arch, Oman: Tectonics, v. 34, p. 488–509, doi:10.1002/2014TC003725.

Tarasewicz, J.P.T., Woodcock, N.H., and Dickson, J.A.D., 2005, Carbonate dilation breccias: Examples from the damage zone to the Dent fault, northwest England: Geological Society of America Bulletin, v. 117, p. 736–745, doi:10.1130/B25568.1.

Tavani, S., Storti, F., Lacombe, O., Corradetti, A., Muñoz, J.A., and Mazzoli, S., 2015, A review of deformation pattern templates in foreland basin systems and fold-and-thrust belts: Implications for the state of stress in the frontal regions of thrust wedges: Earth-Science Reviews, v. 141, p. 82–104.

Tondi, E., Cilona, A., Agosta, F., Aydin, A., Rustichelli, A., Renda, P., and Giunta, G., 2012, Growth processes, dimensional parameters and scaling relationships of two conjugate sets of compactive shear bands in porous carbonate grainstones, Favignana Island, Italy: Journal of Structural Geology, v. 37, p. 53–64, doi:10.1016/j.jsg.2012.02.003.

Torabi, A., and Berg, S.S., 2011, Scaling of fault attributes: A review: Marine and Petroleum Geology, v. 28, p. 1444–1460, doi:10.1016/j.marpetgeo.2011.04.003.

Walsh, J.J., and Watterson, J., 1987, Distributions of cumulative displacement and seismic slip on a single normal fault surface: Journal of Structural Geology, v. 9, p. 1039–1046, doi:10.1016/0191-8141(87)90012-5.

Walsh, J.J., and Watterson, J., 1988, Analysis of the relationship between displacements and dimensions of faults: Journal of Structural Geology, v. 10, p. 239–247, doi:10.1016/0191-8141(88)90057-0.

Warburton, J., Burnhill, T.J., Graham, R.H., and Isaac, K.P., 1990, The evolution of the Oman Mountains foreland basin, *in* Robertson, A.H.F., Searle, M.P., and Ries, A.C., eds., The Geology and Tectonics of the Oman Region: Geological Society of London Special Publication 49, p. 419–427, doi:10.1144/GSL.SP.1992.049.01.26.

Wilkins, S.J., and Gross, M.R., 2002, Normal fault growth in layered rocks at Split Mountain, Utah: Influence of mechanical stratigraphy on dip linkage, fault restriction and fault scaling: Journal of Structural Geology, v. 24, p. 1413–1429, doi:10.1016/S0191-8141(01)00154-7.

Woodcock, N.H., Dickson, J.A.D., and Tarasewicz, J.P.T., 2007, Transient permeability and reseal hardening in fault zones: Evidence from dilation breccia textures, *in* Lonergan, L., Jolly, R.J.H., Rawnsley, K., and Sanderson, D.J., eds., Fractured Reservoirs: Geological Society of London Special Publication 270, p. 43–53, doi:10.1144/GSL.SP.2007.270.01.03.

Science Editor: Aaron J. Cavosie
Associate Editor: Enrico Tavarnelli

Manuscript Received 10 March 2015
Revised Manuscript Received 14 December 2015
Manuscript Accepted 22 January 2016

Printed in the USA

Geological Society of America Bulletin

Anatomy and paleofluid evolution of laterally restricted extensional fault zones in the Jabal Qusaybah anticline, Salakh arch, Oman

F. Balsamo, L. Clemenzi, F. Storti, M. Mozafari, J. Solum, R. Swennen, C. Taberner and C. Tueckmantel

Geological Society of America Bulletin published online 10 February 2016;
doi: 10.1130/B31317.1

Notes